Revised: 25 March 2021 | Accepted: 13 April 2021

DOI: 10.1002/cta.3042

ORIGINAL PAPER

WILEY

Single-stage pulse frequency controlled AC–AC resonant converter for different material vessel induction cooking applications

Srinivas Khatroth | **Porpandiselvi Shunmugam**

Department of Electrical Engineering, National Institute of Technology Warangal, Warangal, India

Correspondence
Srinivas Khatroth, Department of Electrical Engineering, National Institute of Technology Warangal, Warangal, Telangana, India.
Email: srinukhitu@student.nitw.ac.in

Funding information
Department of Science and Technology, Government of India, Grant/Award Numbers: CRG/2018/4568, 09.05.2019

Summary

This paper presents a single-stage AC–AC resonant converter configuration for different material vessel induction cooking. The proposed configuration features input power factor correction, boost operation, and integrated bridge inverter configuration for multiple loads. In this topology the inverter legs are operated at two different frequencies to power induction cooking loads of steel and aluminum vessels. The induction cooking loads are operated at frequencies closer to their respective resonant frequencies. The load powers are independently controlled by pulse frequency modulation (PFM) technique. The proposed topology eliminates the use of electromechanical switches. The proposed single-stage AC–AC resonant converter configuration has been tested with two different vessels of steel and aluminum. The simulation and experimental results of the proposed configuration are in good agreement. This topology offers the advantages of low component count, high efficiency, and suitability for different material induction cooking.

KEYWORDS

induction cooking, multi-output series resonant inverter, pulse frequency control, resonant converter, single stage

1 | INTRODUCTION

Induction heating (IH) applications are widely spreading in different domains like domestic, industrial and medical applications due to contact-less and fast operation, non-polluting nature and high efficiency. Compared to conventional heating methods induction heating is simple and economical.[1] IH operates based on Faraday's laws of electromagnetic induction, like a two winding transformer with secondary shorted. High-frequency alternating currents (ACs) are required for induction heating. Series resonant converters are more popular for induction heating because of their advantages compared to other resonant converters.[2] Generally, single switch, half-bridge and full-bridge series resonant inverters[3] are used for high-frequency AC voltage generation in induction heating.

One of the most popular applications of IH is domestic induction cooking (IC). It is because of safe and rapid heating, cleanliness and controllability. In the literature, a good number of multi-stage and single-stage inverter topologies have been proposed for ferromagnetic material vessels.[4] Control of output power can be achieved by different techniques[5] such as asymmetric duty cycle control (ADC),[6] asymmetric voltage cancelation control(AVC),[7] pulse frequency control,[8,9] phase-shift control (PSC), pulse density modulation and hybrid power control techniques.[10–12] In Lucia

et al.[13] a load-adaptive control is presented for large range of output power control for induction heating. All these control techniques are having their own merits and demerits.

In the past literature, some inverter topologies have been suggested for multi-load induction heating applications. The main requirements of this applications are independent control of the individual load, low component count and high efficiency. An inverter topology with three legs has been proposed in Burdio et al.[14] for powering two IH loads. One leg is common for both loads. It offers less component count, high efficiency and independent control with AVC. In Forest et al.[15] a multi-output inverter configuration is proposed for IC applications. It is suitable for low power applications as it uses a half-bridge configuration. Independent power control of multiple loads is obtained through variable frequency control method. Electromechanical switches are used to connect the loads and resonant capacitors. The use of mechanical switches and more number of capacitors are the major limitations of this method. A multiple load inverter configuration with dual-frequency operation for IC is proposed in Papani et al.[16] The advantage of this topology is the elimination of massive capacitors compared to the half-bridge configuration. Independent power control of loads are obtained with ADC control technique. In Kumar et al.[17] half-bridge resonant converter with buck-boost operation is proposed for multiple vessel IC. In this configuration, two half-bridges are operated with constant switching frequency and both load powers are controlled using the ADC modulation technique. In Lucia et al.[18] a matrix converter is proposed for multiple IH systems. It has low component count, higher efficiency but complex control. All the above mentioned configurations are having their own advantages and limitations and are suitable for only ferromagnetic material load.

There are few topologies proposed in literature for non-ferromagnetic vessel induction heating. In Millan et al.[19] first and third harmonic resonant inverter tolopogy is proposed for all-metal IH applications. In Hirokawa et al.[20,21] a high-frequency time-sharing dual resonant inverter is proposed for domestic all-metal induction cooking applications. In Yonemori and Kobayashi[22] double heating coil drive induction heating cooker is proposed. In these topologies due to frequency selection and time sharing, additional switching losses occur, which will reduce the heating efficiency. A dual-layer coil topology is proposed in Han et al.[23] for different IH load application. Each coil has half of the total turns density. Hence, it reduces the effective ampere turns available from each winding. In Millan et al.[24] selective harmonic operation is used in half-bridge inverter-based topology. The limitations of this topology are low power factor and high conduction losses in body diode of the switching device. In Park and Jung,[25] series resonant converter with load-adaptive control is proposed for all-metal induction cooking. This method suffers from the drawback of unbalanced switching losses. All these converter topologies are having their own merits and demerits. Single-stage resonant AC–AC converter topologies have been proposed for induction heating applications in the literature.[26–31] Totem pole bridge-less PFC boost rectifier is used in these topologies. They offer advantages of less component count, high efficiency, power factor correction and boost operation but most of these topologies are half-bridge and full-bridge configurations suitable for single load. In Sarnago et al.[32] a three-leg AC–AC boost converter is proposed to power two similar IH loads. The loads are operated at same frequency and optimum AVC control is employed. Wide band gap devices are used to increase the efficiency. In Pérez-Tarragona et al.[33] single-phase boost-type PFC rectifier is analyzed with different modulation strategies for domestic IH applications. In Sarnago et al.[34] a multiple output boost resonant inverter is proposed. In Sarnago et al.[35] ZVS multi-output resonant inverter Architecture for IH is proposed. However, the above mentioned single-stage topologies are limited to heating of only ferromagnetic vessels. Low relative permeability and low specific resistance of nonmagnetic vessels pose a challenge in the induction heating of non-ferromagnetic vessels.

In this paper, a single-stage AC–AC resonant converter configuration, suitable for IC with different material vessels has been proposed. It is capable of powering multiple loads of steel and aluminum vessels. Independent power control is achieved through pulse frequency modulation technique. It offers high efficiency, less component count and high power factor. The block diagram of the conventional IC system is shown in Figure 1A. It contains a rectifier for conversion of utility AC supply to DC, a power factor correction unit and separate inverter circuits for each load. The IH loads are of ferromagnetic material.Block diagram of the proposed configuration is shown in Figure 1B, which contains single-stage AC–AC converter which powers steel and aluminum vessels. The IH load equivalent circuit is shown in Figure 1C. R_{eq} is equivalent resistance and L_{eq} is equivalent inductance of the IC load as referred to the coil side. It contains a rectifier for conversion of utility AC supply to DC, a power factor correction unit and separate inverter circuits for each load. The IH loads are of ferromagnetic material. This paper is organized as follows. Section 2 presents circuit configuration, principle of operation of the proposed topology. Section 3 explains control technique and different modes of operation. Section 4 describes prototype implementation and experimental results. Independent power control of multi-load is presented in Section 5. Section 6 summarizes this paper with conclusions.

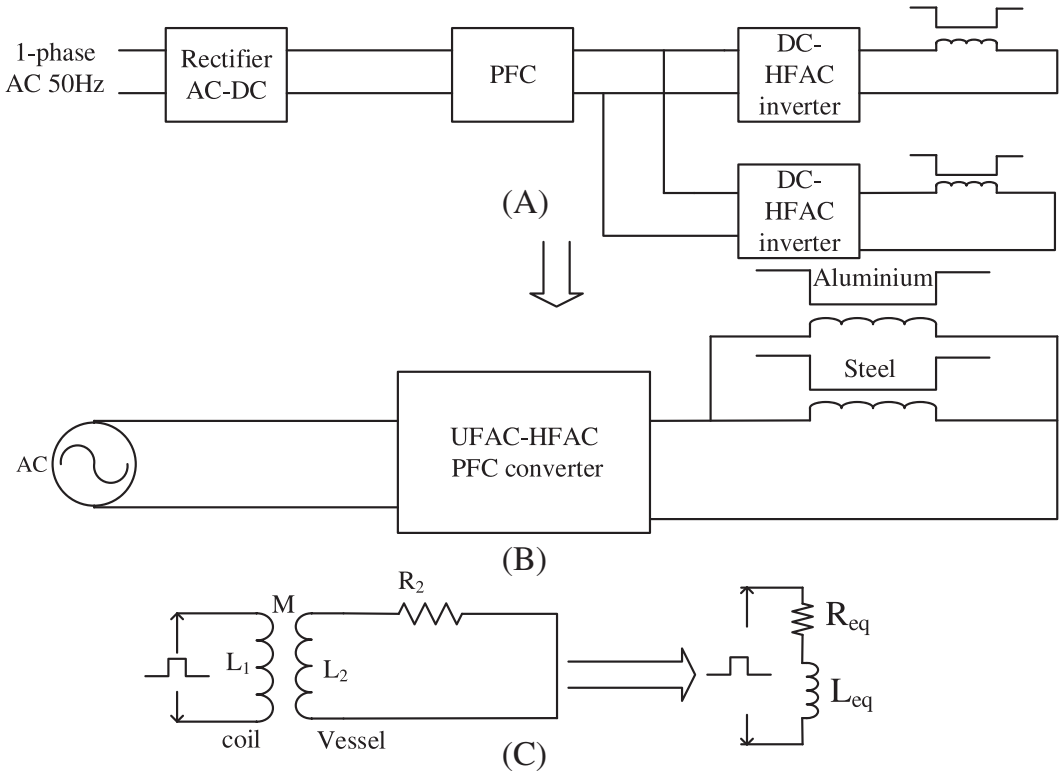

FIGURE 1 Structure of multi-load induction cooking. (A) Two-stage conventional converter. (B) Proposed multi-load single-stage AC–AC converter. (C) Load equivalent circuit

2 | PROPOSED CONVERTER CONFIGURATION

2.1 | Circuit description

The proposed single-stage resonant converter configuration suitable for two different material vessels is shown in Figure 2. The proposed configuration consists of bridge-less boost rectifier and integrated half-bridge resonant inverter circuit. A boost inductor L_b is connected in series with utility frequency AC supply and a DC-link capacitor C_b is connected across inverter leg to ensure the smooth operation of resonant converter. The voltage across C_b is the DC-link voltage v_b. The boost inductor L_b contributes to boosting of utility frequency source voltage V_s. Diodes D_l and D_h form the rectifier branch. In this multi-frequency converter, one leg operates at low-frequency l_f which is suitable for a steel vessel and another leg operates at high-frequency h_f which is suitable for an aluminum vessel. Switching devices S_1 and S_2 are connected in low-frequency leg, switching devices S_3 and S_4 are connected in high-frequency leg. Switching pulses of these inverter devices, corresponding output voltage v_o and both vessel load currents i_{lf} and i_{hf} are shown in Figure 3. Low-frequency leg switches S_1 and S_2 are common for both rectification as well as inverter operation. This common leg devices duty cycle (d) is fixed at 0.5 to get maximum voltage across DC-link due to its boost operation. Lossless snubber capacitors C_{s1}–C_{s4} are connected across switching devices S_1–S_4, respectively, which help in ZVS operation. D_1–D_4 are anti-parallel diodes of the devices S_1–S_4, respectively. The inverter output voltage is supplied to two IH loads. R_{lf} and L_{lf} are the equivalent resistance and equivalent inductance of steel IH load. C_{rl} is the external resonant capacitor. R_{hf} and L_{hf} are the equivalent inductance and resistance of aluminum IH load and C_{rh} is the external resonant capacitor. The corresponding resonant frequencies are f_{rl} and f_{rh}, respectively. The switching frequencies are selected as $f_l = 20$ kHz and $f_h = 160$ kHz. The admittance curves of two IH resonant loads are shown in Figure 4. As shown in Figure 3, v_o is sum of low- and high-frequency voltage components. Low-frequency current i_{lf}, flows through the steel IH load and high-frequency current i_{hf} flows through the aluminum IH load.

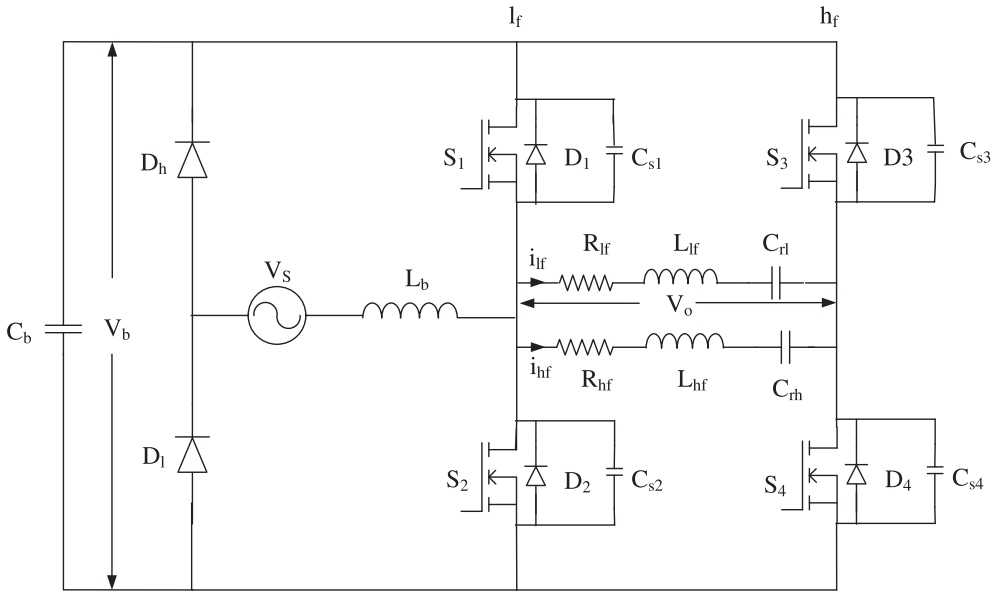

FIGURE 2 Proposed converter configuration

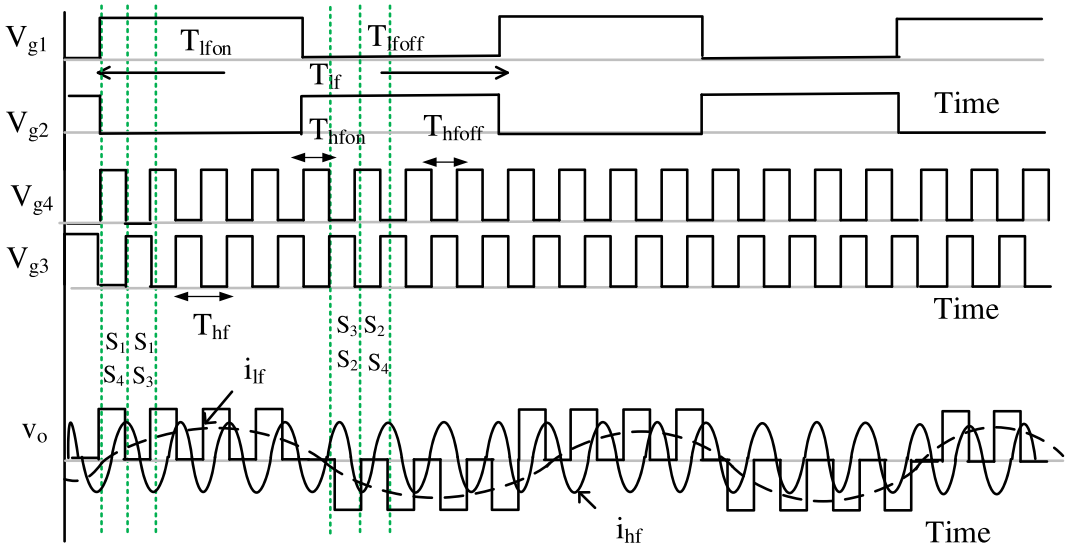

FIGURE 3 Inverter switching pulses and output voltage and load currents

2.2 | Selection of switching frequencies

In general, for IH with ferromagnetic material, switching frequency is selected above 20 kHz. Whereas non-ferromagnetic materials need high switching frequencies due to their low relative permeability and low specific resistance. Equation (1) shows the expression for skin depth (δ), where f_s is the switching frequency, ρ is the specific resistivity and μ is permeability of the material. Operation at high frequencies helps in reducing the skin depth and thereby increases effective resistance. By increasing effective resistance of non-ferromagnetic material, the current drawn from the source is reduced to a safe value.

$$\delta = \sqrt{\frac{\rho}{\pi \mu f_s}} \tag{1}$$

In induction cooking applications, the high-frequency range is normally selected as 100–200 kHz, to limit the inverter switching losses.Characteristics of different IH loads are plotted in Figure 5. Frequency characteristics of steel and aluminum vessel loads are shown in Figure 5A,B. From these figures it is observed that there is a change in inductance and resistance of IH load with frequency. For steel vessel IH load, the switching frequency (f_l) is selected as 20 kHz. From Figure 5B, it is observed that beyond 140 kHz, the equivalent resistance of aluminum vessel IH load increases above 1Ω. Hence, the switching frequency (f_h) is selected as 160 kHz which is an even multiple of low switching frequency (f_l). This frequency ratio of eight will help in independent control of different loads. At switching frequency of 20 kHz, equivalent resistance is 2.2 Ω and equivalent inductance is 68.2 μH for steel vessel IH load. At 160 kHz, equivalent resistance is 1.35 Ω and equivalent inductance is 50.7 μH for aluminum vessel IH load. To facilitate ZVS operation, $\frac{f_s}{f_r}$ ratio has to be selected closer to 1.1. Hence, f_{rl} and f_{rh} are selected as 18.4 and 158 kHz, respectively. The expressions for f_{rl} and f_{rh} are $f_{rl} = \frac{1}{2\Pi\sqrt{L_{lf}C_{rl}}} f_{rh} = \frac{1}{2\Pi\sqrt{L_{hf}C_{rh}}}$, respectively. Admittance characteristics of different IH loads are shown in Figure 4. It shows that steel vessel IH resonant load offers maximum admittance to low-frequency current and aluminum vessel IH resonant load offers maximum admittance to high-frequency current.

2.3 | Operating principle

The proposed single AC–AC converter configuration is the combination of series resonant load inverter and boost converter. In this configuration, as shown in Figure 2, one inverter leg is common for both boost and series inverter operation.

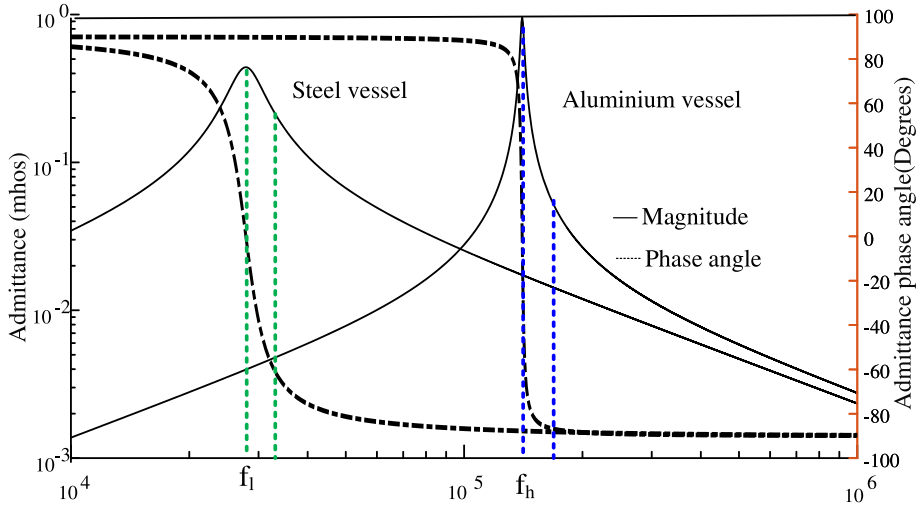

FIGURE 4 Admittance curve

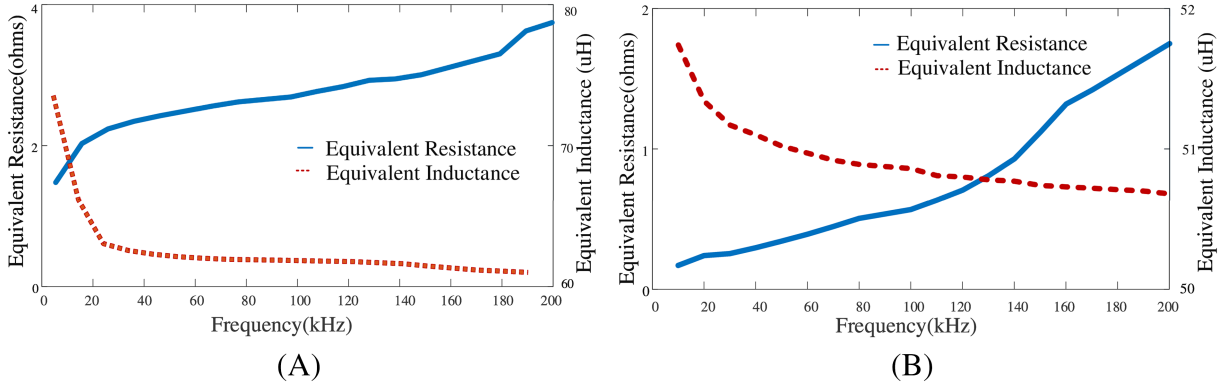

FIGURE 5 IH load frequency characteristics. (A) Steel vessel. (B) Aluminum vessel

The volt–sec balance across boost inductor L_b,Expression of I_{Lbpeak}.The boost operation is described through Equations (1)–(5)[32]

$$V_s dT_s + (V_s - v_b)(1-d)T_s = 0 \tag{2}$$

where T_s is the time period corresponding to the common leg (leg-1) frequency, that is, l_f. Expression of L_b for continuous conduction is

$$L_b > \frac{V_b - v_s}{I_{Lbpeak}}(1-d)T_s \tag{3}$$

where

$$I_{Lbpeak} = I_{Lb} + \frac{\Delta I_{Lb}}{2} \tag{4}$$

By neglecting the source current ripple, the average value of DC-link voltage v_b can be expressed as

$$v_b = \frac{V_s}{(1-d)} \tag{5}$$

From Equation (5), it is observed that due to boost operation there is an increase in DC-link voltage v_b which leads to increase in v_o also. Two IH resonant loads are connected across low- and high-frequency legs of the inverter.

At low frequency, steel vessel load impedance can be expressed as

$$Z_{eqlf} = R_{lf} + j(X_{Llf} - X_{Clf}) \tag{6}$$

where

$$X_{Llf} = 2\pi f_l L_{lf},\ X_{clf} = \frac{1}{2\pi f_l C_{rl}}$$

At high frequency, aluminum vessel load impedance can be expressed as

$$Z_{eqhf} = R_{hf} + j(X_{Lhf} - X_{Chf}) \tag{7}$$

where

$$X_{Lhf} = 2\pi f_h L_{hf},\ X_{Chf} = X_{clf} = \frac{1}{2\pi f_h C_{rh}}$$

Inverter output voltage across load v_o is the combination of low- and high-frequency voltage components, v_{lf} and v_{hf} as shown in Figure 3. Hence, v_o can be represented as a series connection of two voltage sources v_{lf} and v_{hf} as shown in Figure 6A.

$$v_0 = v_{lf} + v_{hf} \tag{8}$$

Figure 6B shows the load equivalent circuit for low-frequency component of v_o. At f_l, the reactance of C_{rh} is very high, and hence, it behaves like open circuit. However, the low-frequency load offers low impedance at this frequency and i_{lf} flows through this load as shown in Figure 6B. Figure 6C shows the load equivalent circuit for high-frequency component of v_o. At f_h, the reactance of L_{lf} is very high, and hence, it behaves as an open circuit. However, the high-frequency load offers low impedance, and hence, i_{hf} flows through this load as shown in Figure 6C. Hence, in response

to the output voltage v_o, only a low-frequency current i_{lf} flows through steel vessel load and a high-frequency current i_{hf} flows through aluminum vessel load. Figure 6A. shows the waveforms and FFT of these currents.

2.4 | Output power analysis

The output power to steel vessel is calculated as $I_{lf}^2 R_{lf}$, that is, real power consumption by equivalent resistance of steel vessel load. The output power to aluminum vessel is calculated as $I_{hf}^2 R_{hf}$, that is, real power consumption by equivalent resistance of aluminum vessel load. I_{lf} is RMS value of low-frequency current and I_{hf} is RMS values of high-frequency currents. The output power(P_o) of the inverter is expressed as

$$P_0 = P_{lf} + P_{hf} \tag{9}$$

where

$$\begin{aligned} P_{lf} &= \text{steel load output power} = I_{lf}^2 R_{lf} \\ P_{hf} &= \text{aluminium load output power} = I_{hf}^2 R_{hf} \end{aligned}$$

3 | MODES OF OPERATION

The proposed converter operation can be described in eight different modes. Modes 1 to 8 are obtained for positive (+ve) half cycle of the utility frequency AC supply voltage and modes 9 to 16 are obtained with negative(−ve) half cycle of the source voltage.

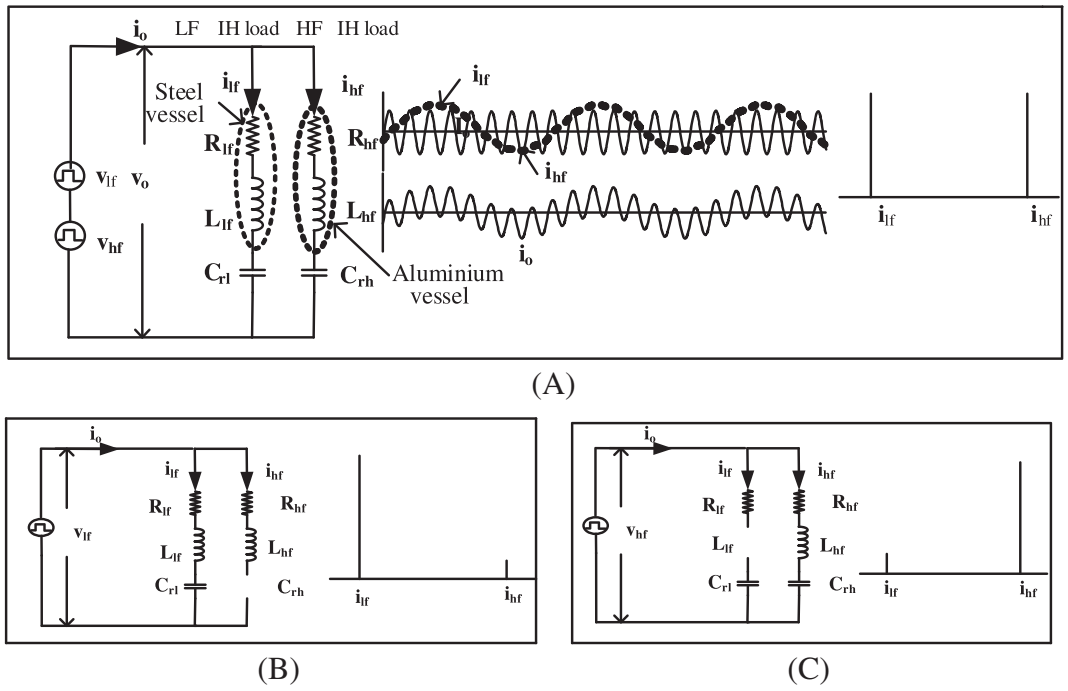

FIGURE 6 Load equivalent circuit, load currents and FFT. (A) Load equivalent circuit of multi-frequency converter, load currents, and FFT. (B) Load equivalent circuit for v_{lf} and load current FFT. (C) Load equivalent circuit for v_{hf} and load current FFT

Mode 1: During this mode, the supply voltage is positive (+ve) and the devices S_1 and S_4 are ON. Figure 7A shows the corresponding equivalent circuit. Source current i_s flows through the path of V_S–D_h–S_1–L_b and boost inductor L_b stores the energy. During this interval, the output current i_o is positive and flows through the path of S_1–load–S_4–C_b. DC-link capacitor C_b discharges. The inverter output voltage is $+v_b$. Expression for load voltage and load currents are expressed through Equations (10)–(17)[16]

$$v_0 = v_b + v_{crl}(t = 0 \text{ or } t_{n-1}) \tag{10}$$

$$v_0 = L_{lf}\frac{di_{lf}(t)}{dt} + \frac{1}{C_{rl}}\int i_{lf}(t)dt + v_{crl}(t = 0 \text{ or } t_{n-1}) + i_{lf}(t)R_{lf} \tag{11}$$

low-frequency current

$$i_{lf}(t) = \frac{v_0 - v_{crl}(t = 0 \text{ or } t_{n-1})}{\omega_n L_{lf}} e^{-\alpha t}\sin\omega_n t + i_{lf}e^{-\alpha t}\left(\cos\omega_n t - \frac{\alpha}{\omega_n}\sin\omega_n t\right) \tag{12}$$

$$v_{crl}(t) = v_{crlo} + v_0 - v_{crl}(t = 0 \text{ or } t_{n-1})\left(1 - e^{-\alpha t}\left(\cos\omega_n t - \frac{\alpha}{\omega_n}\sin\omega_n t\right)\right) + \frac{i_{lf}(t = 0 \text{ or } t_{n-1})}{\omega_n C_{rl}} e^{-\alpha t}\sin\omega_n t \tag{13}$$

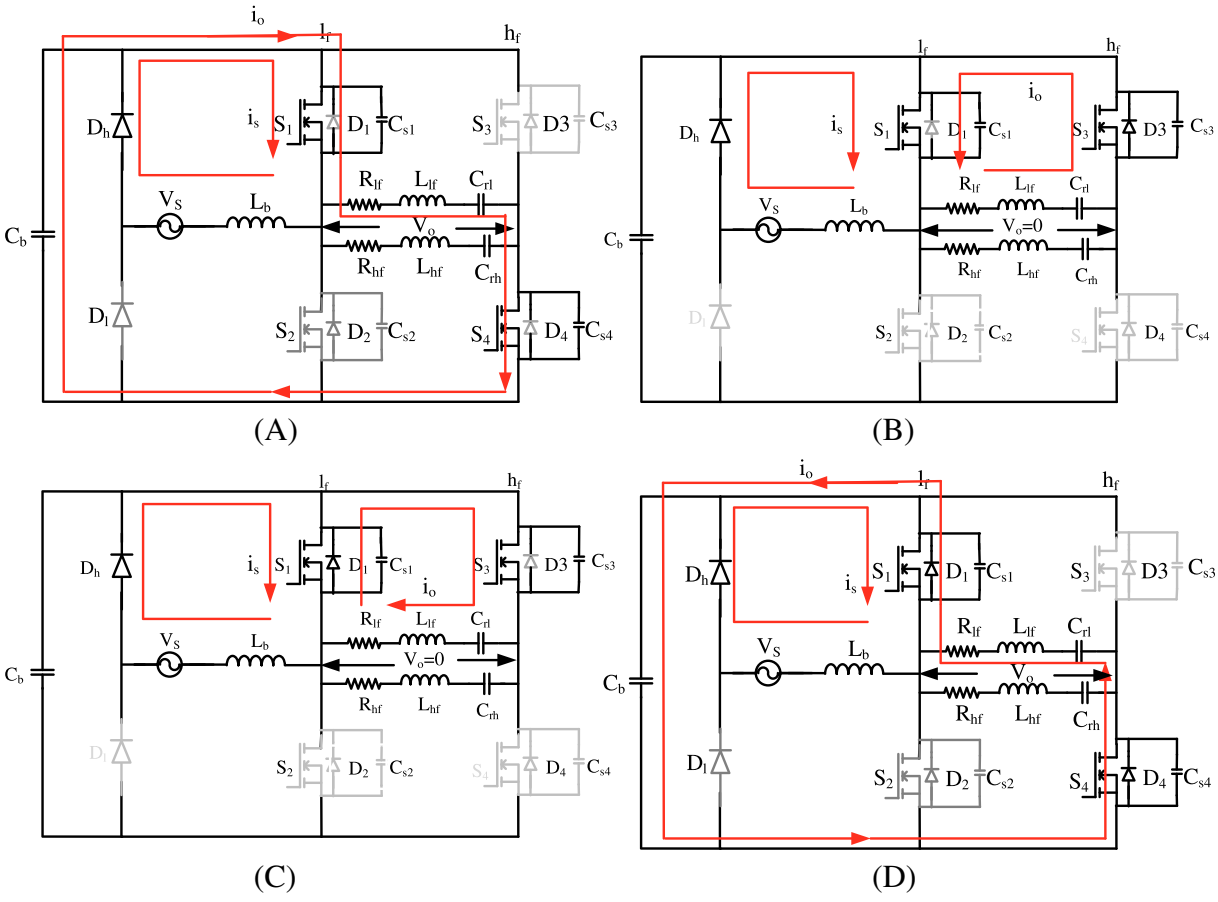

FIGURE 7 Single-stage resonant converter equivalent circuits for mode 1 to mode 4 for $V_s > 0$ (positive half cycle). (A) Mode1 S_1 and S_4 are ON. (B) Mode2 S_1 and S_3 are ON. (C) Mode3 S_3 and S_1 are ON. (D) Mode4 S_4 and S_1 are ON

where

$$\alpha = \frac{R_{lf}}{2L_{lf}} \text{ and } \omega_n = \frac{1}{\sqrt{L_{lf}C_{rl}}}$$

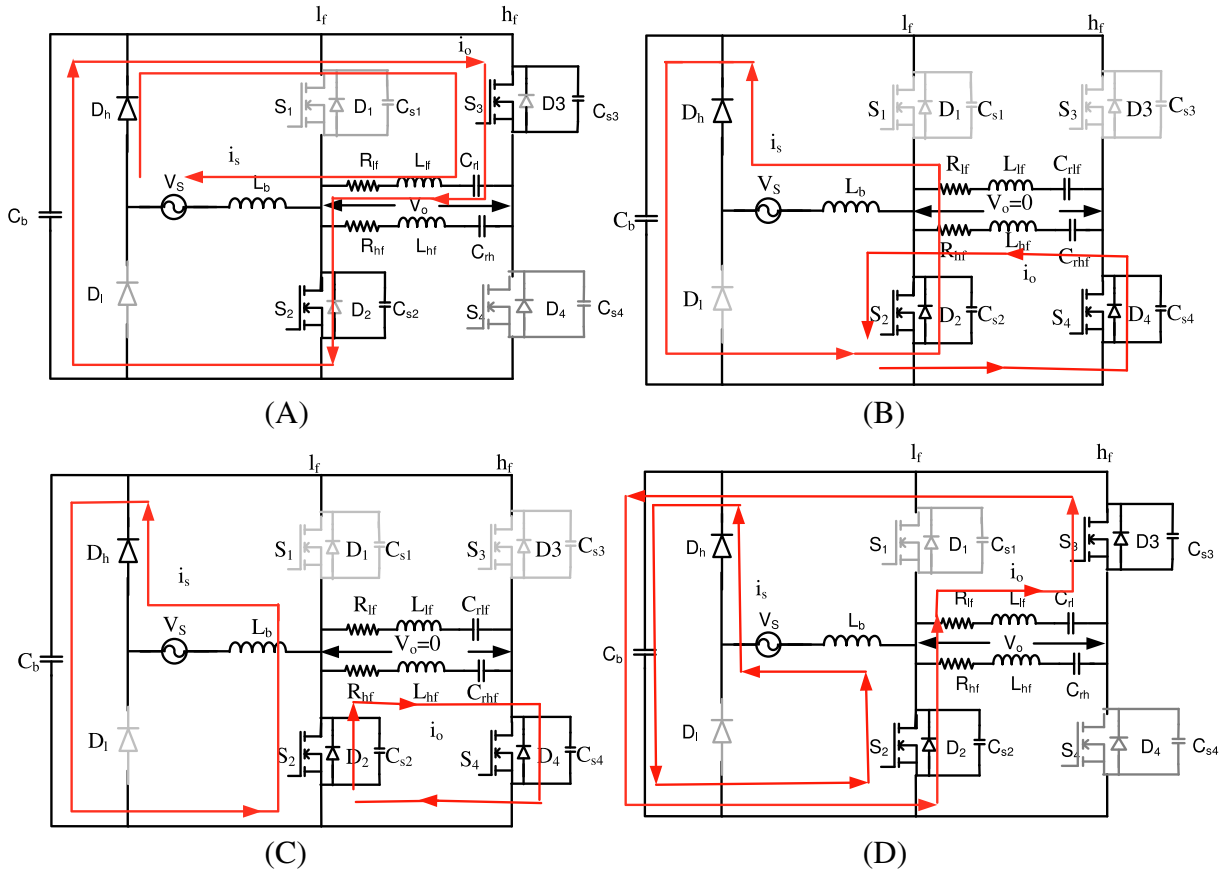

FIGURE 8 Single-stage resonant converter equivalent circuits mode 5 to mode 8 for $V_s > 0$ (positive half cycle) (A) Mode5 S_3 and S_2 are ON. (B) Mode6 S_4 and S_2 are ON. (C) Mode7 S_2 and S_4 are ON. (D) Mode8 S_2 and S_3 are ON

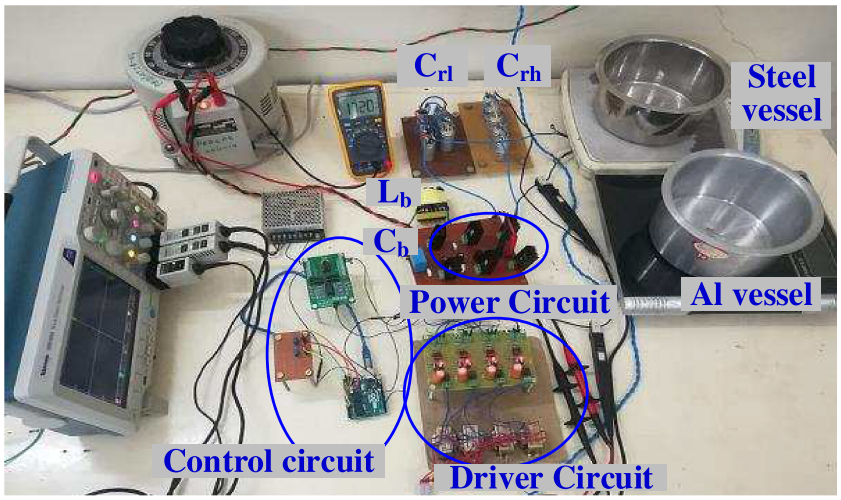

FIGURE 9 Prototype of experimental setup

similarly

$$v_0 = v_b + v_{crh}(t = 0 \text{ or } t_{n-1}) \tag{14}$$

$$v_0 = L_{hf}\frac{di_{hf}(t)}{dt} + \frac{1}{C_{rh}}\int i_{hf}(t)dt + v_{crh}(t = 0 \text{ or } t_{n-1}) + i_{hf}(t)R_{hf} \tag{15}$$

low-frequency current

$$i_{hf}(t) = \frac{v_0 - v_{crh}(t = 0 \text{ or } t_{n-1})}{\omega_n L_{hf}} e^{-\alpha t}\sin\omega_n t + i_{hf}e^{-\alpha t}\left(\cos\omega_n t - \frac{\alpha}{\omega_n}\sin\omega_n t\right) \tag{16}$$

$$v_{crh}(t) = v_{crho} + v_0 - v_{crh}(t = 0 \text{ or } t_{n-1})\left(1 - e^{-\alpha t}\left(\cos\omega_n t - \frac{\alpha}{\omega_n}\sin\omega_n t\right)\right) + \frac{i_{hf}(t = 0 \text{ or } t_{n-1})}{\omega_n C_{rh}} e^{-\alpha t}\sin\omega_n t \tag{17}$$

where

$$\alpha = \frac{R_{hf}}{2L_{hf}} \text{ and } \omega_n = \frac{1}{\sqrt{L_{hf}C_{rh}}}$$

Hence, the instantaneous value of load current

$$i_0(t) = i_{lf}(t) + i_{hf}(t) \tag{18}$$

Equations (10)–(17) are applicable for all remaining modes where the final quantities of previous mode become initial values of the next mode.

At the end of mode-1, i_o becomes positive(+ve).

TABLE 1 Parameters of hardware prototype

Parameter	Value
AC input voltage (V_s)	40 V (max)
Boost inductor	400 μH
DC-link capacitor	6.8 μF
Low-frequency IC load equivalent inductance (L_{lf})	68.2 μH
Low-frequency IC load equivalent resistance (R_{lf})	2.09 Ω
Low-frequency load resonant capacitor (C_{rl})	1.205 μF
High-frequency IC load equivalent inductance (L_{hf})	50.737 μH
High-frequency IC load equivalent resistance (R_{hf})	1.35 Ω
High-frequency load resonant capacitor (C_{rh})	0.0202 μF
Leg-1 switching frequency (f_l)	20 kHz
Low-frequency IH load resonant frequency(f_{rl})	18.4 kHz
Leg-2 switching frequency (f_h)	160 kHz
High-frequency IH load resonant frequency (f_{rh})	158 kHz
MOSFETs used	IRFB4227pbf
Rds,on	19 mΩ
Control board	arduino
Diodes used	VS60EPS
Snubber capacitors	2 nF

Mode 2: During this mode, devices S_1 and S_3 are ON and Figure 7B shows the corresponding equivalent circuit. Source current i_s flows through the path of V_S–D_h–S_1–L_b. The output current is positive and freewheels through S_3 and S_1. Inverter output voltage v_o is 0.

Mode 3: During this mode, devices S_1 and S_3 are ON and Figure 7C shows the corresponding equivalent circuit. Source current i_s flows through the path of V_S–D_h–S_1–L_b. The output current is negative and flowing through D_1, S_3 and load. The load voltage v_o is 0.

Mode 4: During this mode, devices S_1 and S_4 are ON. Figure 7D shows the corresponding equivalent circuit. Source current i_s flows through the path of V_S–D_h–S_1–L_b and boost inductor L_b stores the energy. During this interval, the output current i_o is negative and flows through the path of S_4–load–S_1–C_b and DC-link capacitor C_b charges. The inverter output voltage is $+v_b$.

Mode 5: During this mode, the supply voltage is positive and the devices S_2 and S_3 are ON and Figure 8A shows the corresponding equivalent circuit. Source current i_s flows through the path of V_s–D_h–S_3–load–L_b and boost inductor L_b releases magnetic energy to load. DC-link capacitor C_b discharges through S_3,load, S_2. The inverter output voltage is $-v_b$ and i_o is negative.

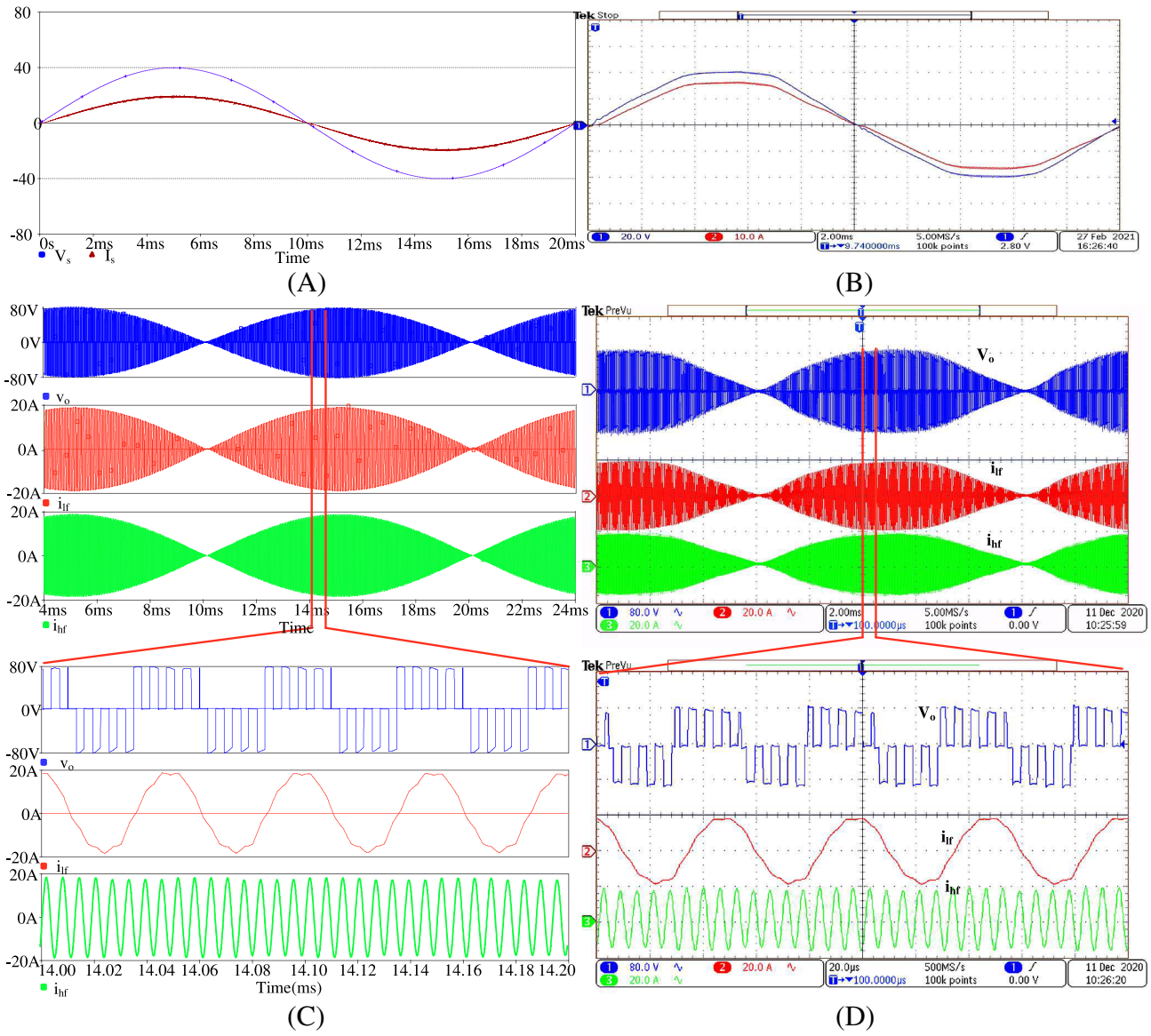

FIGURE 10 Simulated and experimental waveforms of V_s, i_s, v_o, i_{lf}, and i_{hf}. (A) Simulated waveforms of source voltage and source current. (B) Experimental waveforms of source voltage and source current. (C) Simulated waveforms of output voltage and low- and high-frequency load currents at $f_l = 20$ kHz and at $f_h = 160$ kHz. (D) Experimental waveforms of load voltage and low- and high-frequency load currents at $f_l = 20$ kHz and at $f_h = 160$ kHz

Mode 6: During this mode, devices S_2 and S_4 are ON and Figure 8B shows the corresponding equivalent circuit. Source current i_s flows through the path of V_s–D_h–C_b–S_2–L_b. i_o is negative and flows through the path of load–S_2–D_4. DC-link capacitor C_b is charging. Inverter output voltage v_o is 0.

Mode 7: During this mode, devices S_2 and S_4 are ON and Figure 8C shows corresponding equivalent circuit. Source current i_s flows through the path of V_s–D_h–C_b–S_2–L_b. i_o is positive and flows through the path of load–S_4–D_2. DC-link capacitor C_b discharges. Inverter output voltage v_o is 0.

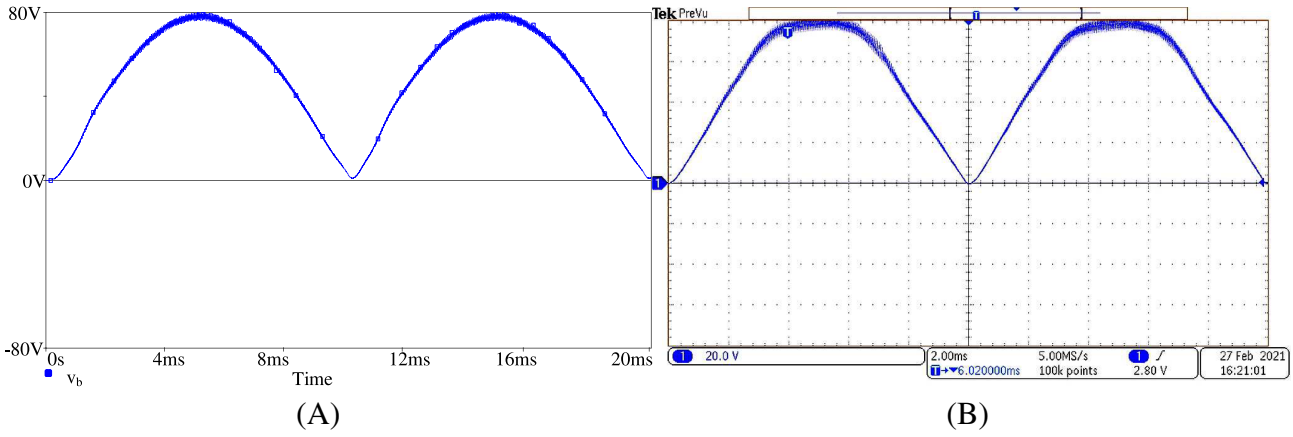

FIGURE 11 Simulated and experimental waveforms of DC-link capacitor Voltage. (A) Simulated waveform of DC-link capacitor voltage. (B) Experimental waveform of DC-link capacitor voltage

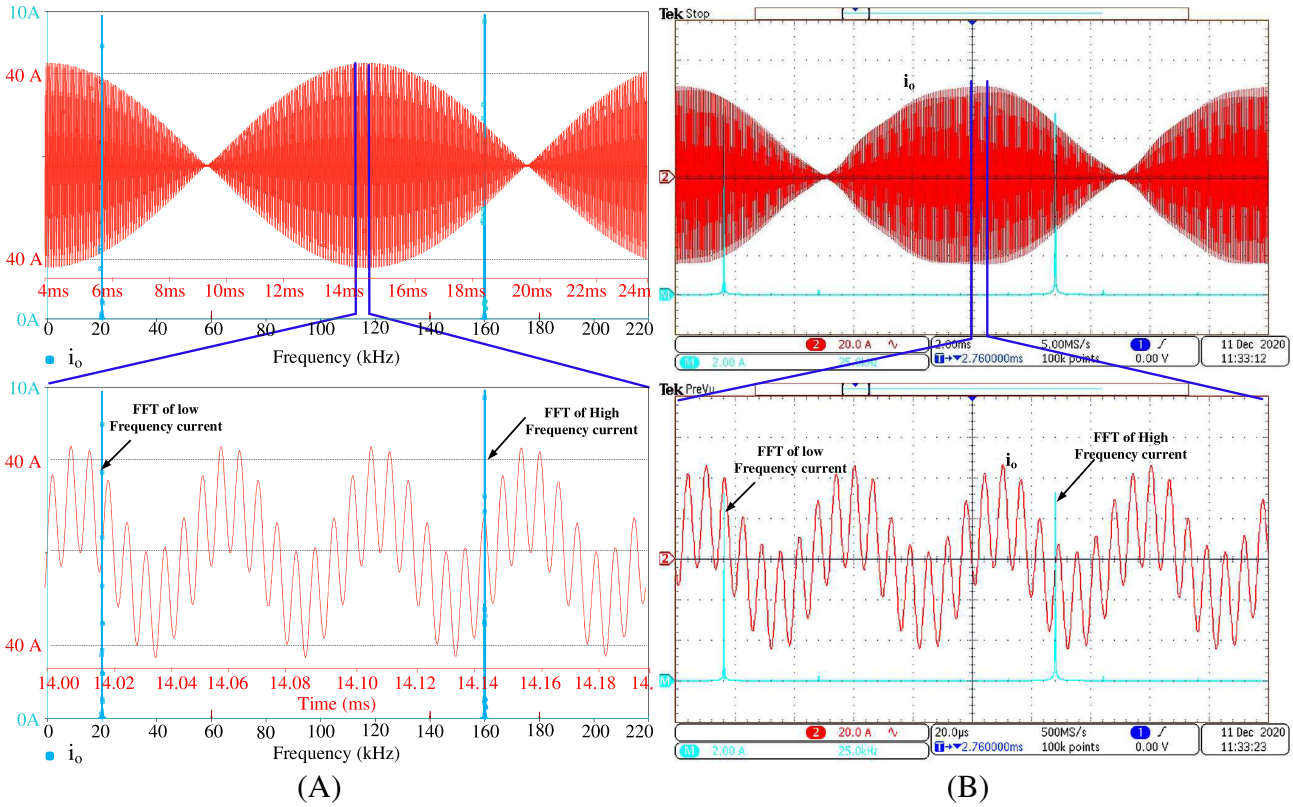

FIGURE 12 Simulated and experimental waveforms of i_o and its FFTs for $f_l = 20$ kHz and $f_h = 160$ kHz. (A) Simulated waveform of total output current and its FFT. (B) Experimental waveform of total output current and its FFT

Mode 8: During this mode, devices S_2 and S_3 are ON and Figure 8D shows corresponding equivalent circuit. Source current i_s flows through the path of V_s–D_h–C_b–S_2–L_b. i_o is positive and flows through the path of load–S_3–C_b–S_2. DC-link capacitor C_b charges. The inverter output voltage is $-v_b$.

During the supply voltage negative half cycle ($V_s < 0$), the operation consists of 8 modes which are similar to that of the modes existing for the positive half cycle with changes in conducting elements due to polarity reversal. D_h is off and D_l is on during this negative half cycle.

4 | SIMULATION AND EXPERIMENTAL RESULTS

A 316 W prototype of a single-stage resonant converter has been implemented for induction cooking with two different material vessels. The implemented prototype is shown in Figure 9. The converter circuit parameters are described in Table 1. The AC input voltage $V_s = 40$ V (max) and frequency $f = 50$ Hz. The load parameters are measured from the coil side with the practical domestic cooking vessels of steel and aluminum kept over the IH coils. Switching frequencies of converter legs 1 and 2 are selected as 20 and 160 kHz, respectively. The low and high resonant frequencies are set as 18.4 and 158 kHz, respectively, by using suitable values of resonant capacitors. The simulation and experimental results at different switching frequencies are shown in Figures 10–16). Figure 10 shows the simulated and experimental results of source voltage (V_s), source current (i_s), inverter output voltage v_o, low-frequency output current i_{lf}, high-frequency output current i_{hf} at $f_l = 20$ kHz and $f_h = 160$ kHz. The simulated and experimental results are in good agreement with each other. Figure 10A,B shows, respectively, simulated and experimental waveforms of V_s and i_s. From these waveforms it can be observed that supply voltage V_s and current i_s are in phase and the proposed converter operates at unity power factor. Figure 10C,D show, respectively, simulated and experimental waveforms of v_o, i_{lf} and i_{hf}. Figure 11A,B show the simulated and experimental waveforms of DC-link voltage v_b at $f_l = 20$ kHz and $f_h = 160$ kHz. It

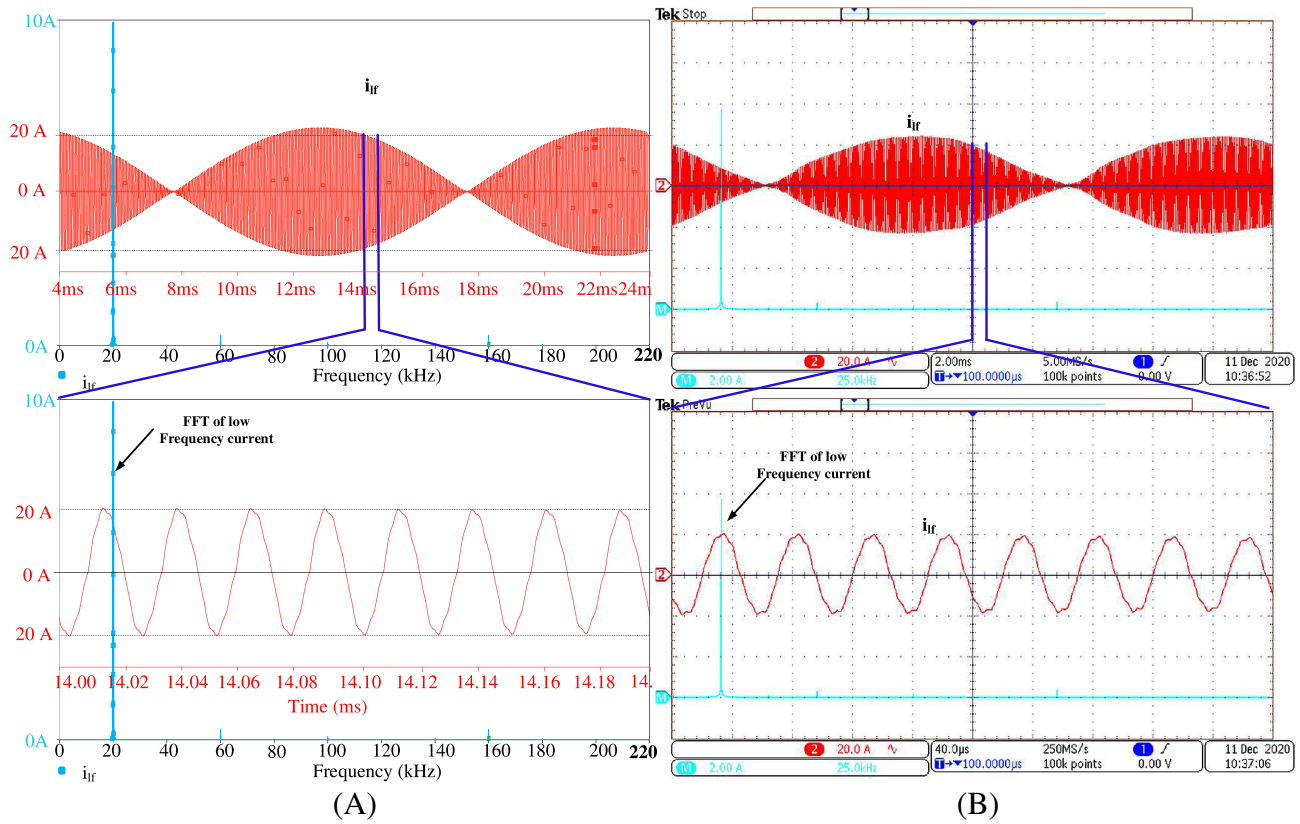

FIGURE 13 Simulated and experimental waveforms of i_{lf} and its FFTs for $f_l = 20$ kHz. (A) Simulated waveform of low-frequency load current and its FFT. (B) Experimental waveform of low-frequency load current and its FFT

is observed that the peak value of the DC-link voltage is 80 V when the peak value of source voltage is 40 V, which indicates the boost operation of the converter. Figure 12 shows simulated and experimental waveforms of total output load current i_o and its FFT with $f_l = 20$ kHz and $f_h = 160$ kHz. Figure 12A show simulated waveforms of total output load current i_o and its FFT. Figure 12B show experimental waveforms of total output load current i_o and its FFT. Figures 13 and 14 show simulated and experimental waveforms of individual load currents FFT with $f_l = 20$ kHz and $f_h = 160$ kHz. Figure 13A show simulated waveforms of low-frequency load current i_{lf} and its FFT, Figure 13B show experimental waveforms of low-frequency load current i_{lf} and its FFT, Figure 14A show simulation waveforms of high-frequency load current i_{hf}. Figure 14B show experimental waveforms of high-frequency load current i_{hf}. From these figures, it is observed that inverter output current contains only low- and high-frequency components of current and the respective frequency current component flows through the corresponding IH load. The low-frequency current component flows through the steel vessel IH load and high-frequency current component flows through the aluminum vessel IH load. From FFTs, it is observed that low-frequency IH load RMS current is $i_{lf} = 9.6$ A and the same for high-frequency IH load is $i_{hf} = 9.56$ A. Output power control is achieved using pulse frequency control. Figures 15 and 16 show the simulated and experimental waveforms of total output current i_o and its FFT for different combinations of f_l and f_h. Figure 15A,B show simulation and experimental waveforms of i_o and its FFT at $f_l = 25$ kHz and $f_h = 160$ kHz. It is observed that low-frequency load RMS current is reduced to $I_{lf} = 4.2$ A and high-frequency load RMS current remains unchanged at $I_{hf} = 9.56$ A as only low switching frequency is increased. Figure 16A,B show simulated and experimental waveforms of i_o and its FFT at $f_l = 20$ kHz and $f_l = 165$ kHz. From these figures it can be observed that high-frequency load RMS current is reduced to $I_{hf} = 4.2$ A and low-frequency load RMS current remains at the rated value of $I_{lf} = 9.6$ A. These results depict independent load power control. Low- and high-frequency output powers (P_{lf} and P_{hf}) are controlled by varying corresponding switching frequency. The above results are tabulated in Table 2. The simulated and experimental results are in good agreement with each other. Hence, the proposed converter provides a single-stage AC–AC converter with unity power factor, boost operation, multi-frequency output and independent output power control.

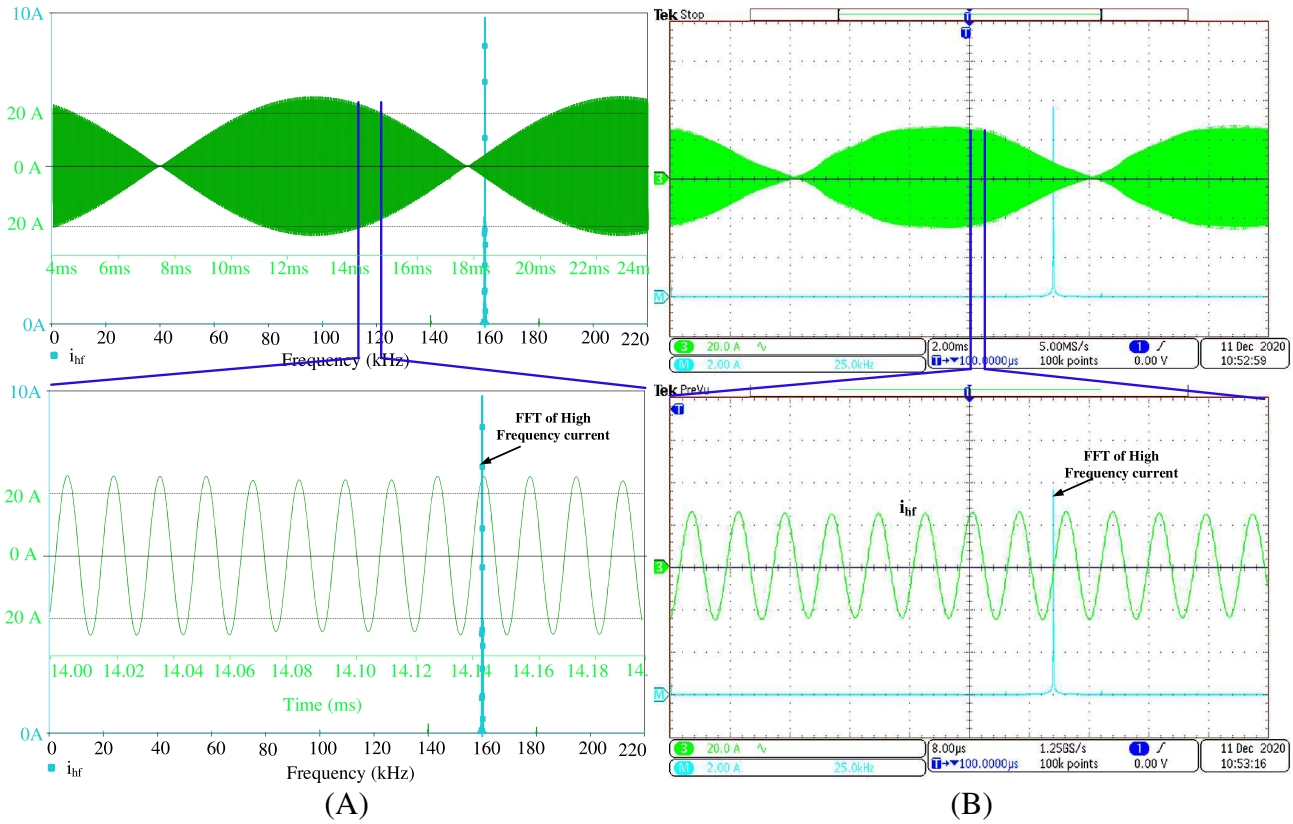

FIGURE 14 Simulated and experimental waveforms of i_{hf} and its FFTs for $f_h = 160$ kHz. (A) Simulated waveform of high-frequency load current and its FFT. (B) Experimental waveform of high-frequency load current and its FFT

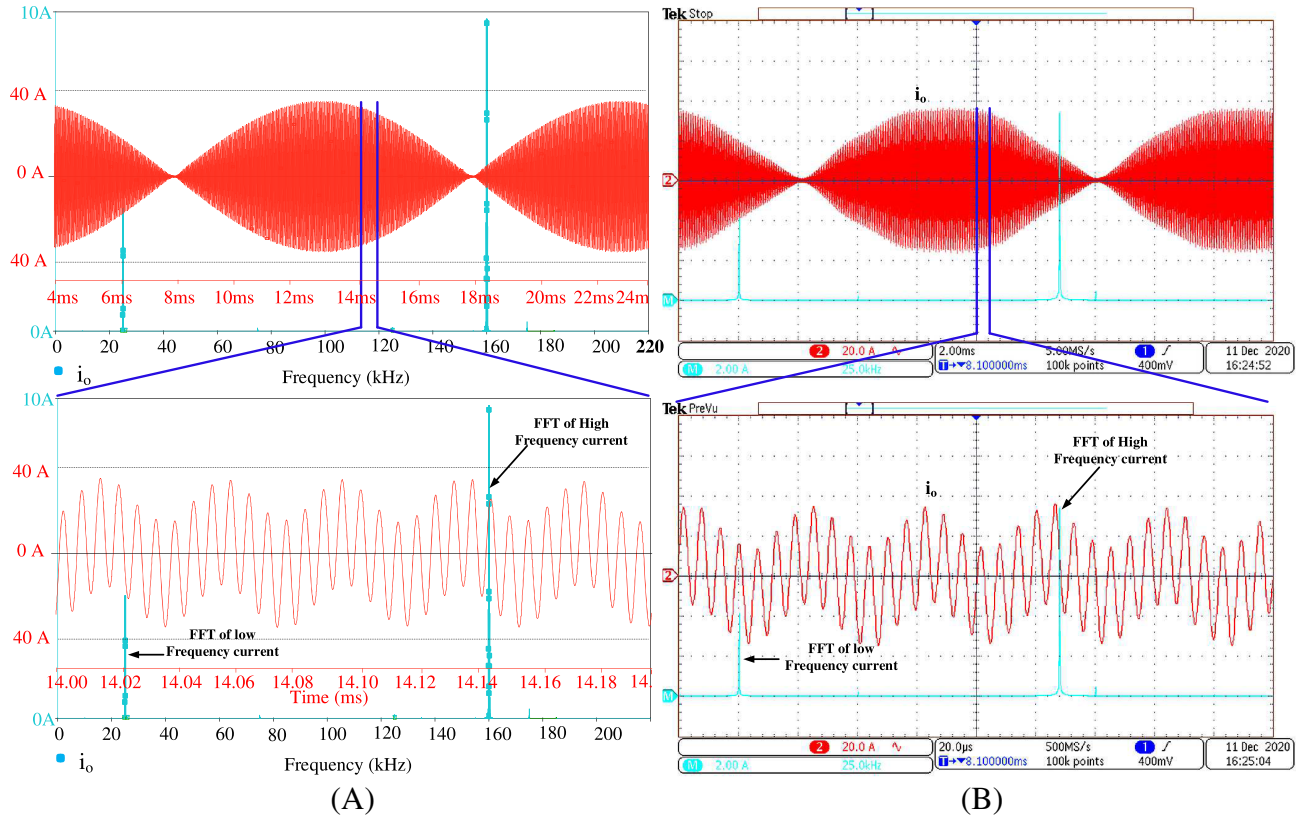

FIGURE 15 Simulated and experimental waveforms of i_o and its FFTs for $f_l = 25$ kHz and $f_h = 160$ kHz. (A) Simulated waveform of total output current and its FFT at $f_l = 25$ kHz and $f_h = 160$ kHz. (B) Experimental waveform of total output current and its FFT at $f_l = 25$ kHz and $f_h = 160$ kHz

5 | ANALYSIS OF RESULTS AND CONVERTER EFFICIENCY

In the proposed single-stage AC–AC converter, power control is obtained through pulse frequency control due its advantages like symmetrical quasi-square wave output voltage, higher conversion efficiency for low and medium range loads and does not require any control-loop-compensation network.[9] Figure 17 shows low- and high-frequency output currents and power control with frequency. Figure 17A shows the variation of simulated and experimental load currents with variation of low switching frequency of leg-1 devices. Figure 17C shows the low- and high-frequency IH load powers with variation of the low switching frequency of leg-1 devices. It can be observed that the low-frequency load current and corresponding output power, that is, of steel vessel, decrease with increase in low switching frequency. The corresponding high-frequency components remain constant. Figure 17B shows the variation of simulated and experimental load currents with variation of high switching frequency of leg-2 devices. Figure 17D shows the low- and high-frequency IH load powers with variation of high switching frequency of leg-2 devices. It can be observed that the high-frequency load current and corresponding power, that is, of aluminum vessel IH load power, decrease with increase in high switching frequency, where the corresponding low-frequency components remain constant. These characteristics prove the independent power control of both low- and high-frequency vessel loads with pulse frequency modulation. The simulated and experimental results are also in good agreement. Hence, the proposed inverter is suitable for heating steel and aluminum vessels simultaneously with independent control. The low- and high-frequency output powers are obtained using Equations (19) and (20)

$$P_{lf} = V_{olf,rms} I_{olf,rms} \cos \phi_{olf} \approx I_{lf}^2 R_{lf} \tag{19}$$

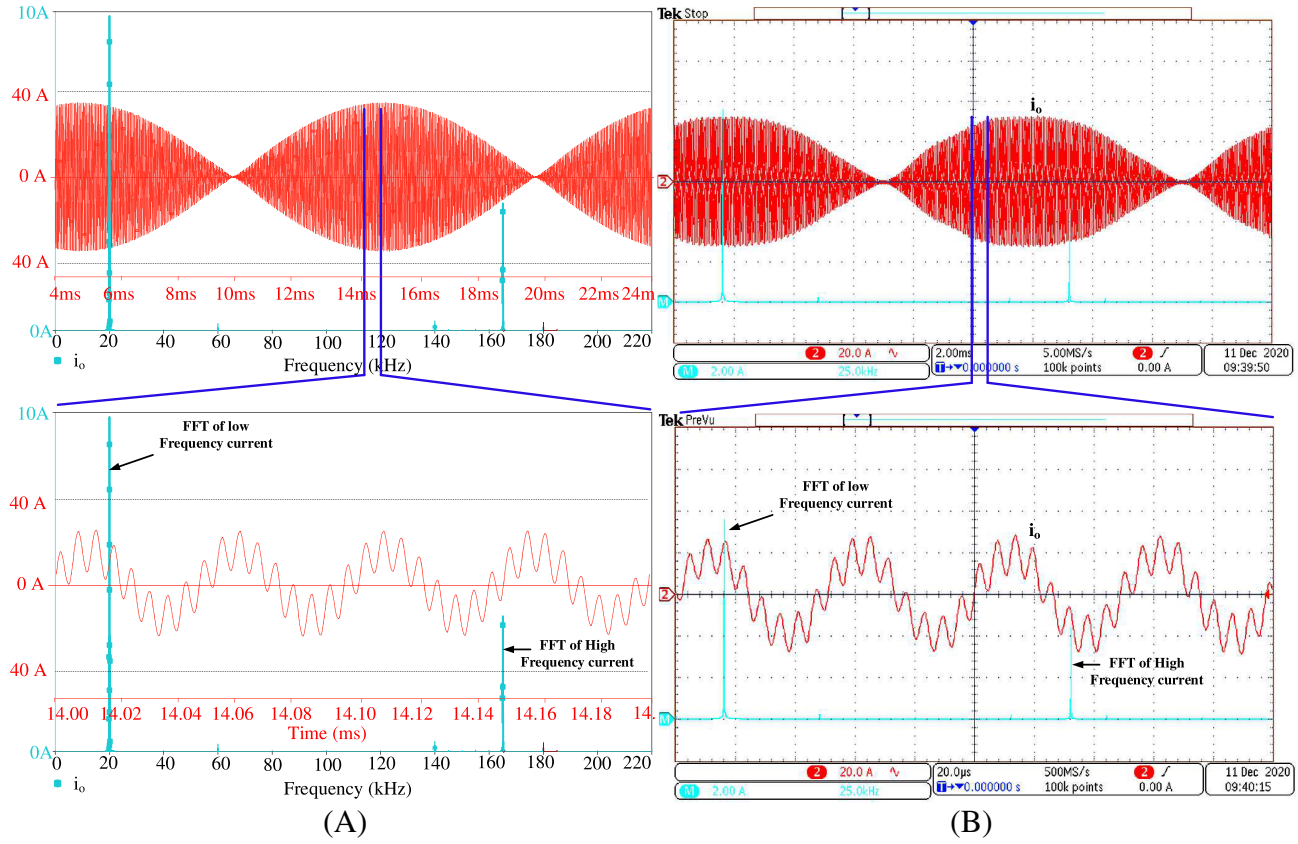

FIGURE 16 Simulated and experimental waveforms of i_o and its FFTs for $f_l = 20$ kHz and $f_h = 165$ kHz. (A) Simulated waveform of total output current and its FFT at $f_l = 20$ kHz and $f_h = 165$ kHz. (B) Experimental waveform of total output current and its FFT at $f_l = 20$ kHz and $f_h = 165$ kHz

V_s (V)	P_{in} (W)	f_l (kHz)	f_h(kHz)	P_{lf} (W)	P_{hf}(W)	P_o(W)	Efficiency
40	340	20	160	192.6	123.4	316	93.2%
40	173.2	25	160	37	123.4	160.4	92.5%
40	235	20	165	192.6	23.8	216.4	92.2%

TABLE 2 Output power and efficiency for different combinations of f_l and f_h

$$P_{hf} = V_{ohf,rms} I_{ohf,rms} \cos\phi_{ohf} \approx I_{hf}^2 R_{hf} \tag{20}$$

The total output power is the sum of output powers of steel vessel load (P_{lf}) and aluminum vessel load (P_{hf}).

$$P_0 = P_{lf} + P_{hf} \tag{21}$$

The input power of the converter is calculated (Equation (22)) as product of RMS input voltage (V_s, rms) and RMS input current (I_s, rms) of the converter as the power factor is closer to unity.

$$P_{in} = V_{s,rms} I_{s,rms} \cos\phi_{in} \approx V_{s,rms} I_{s,rms} \tag{22}$$

Overall converter efficiency is calculated as

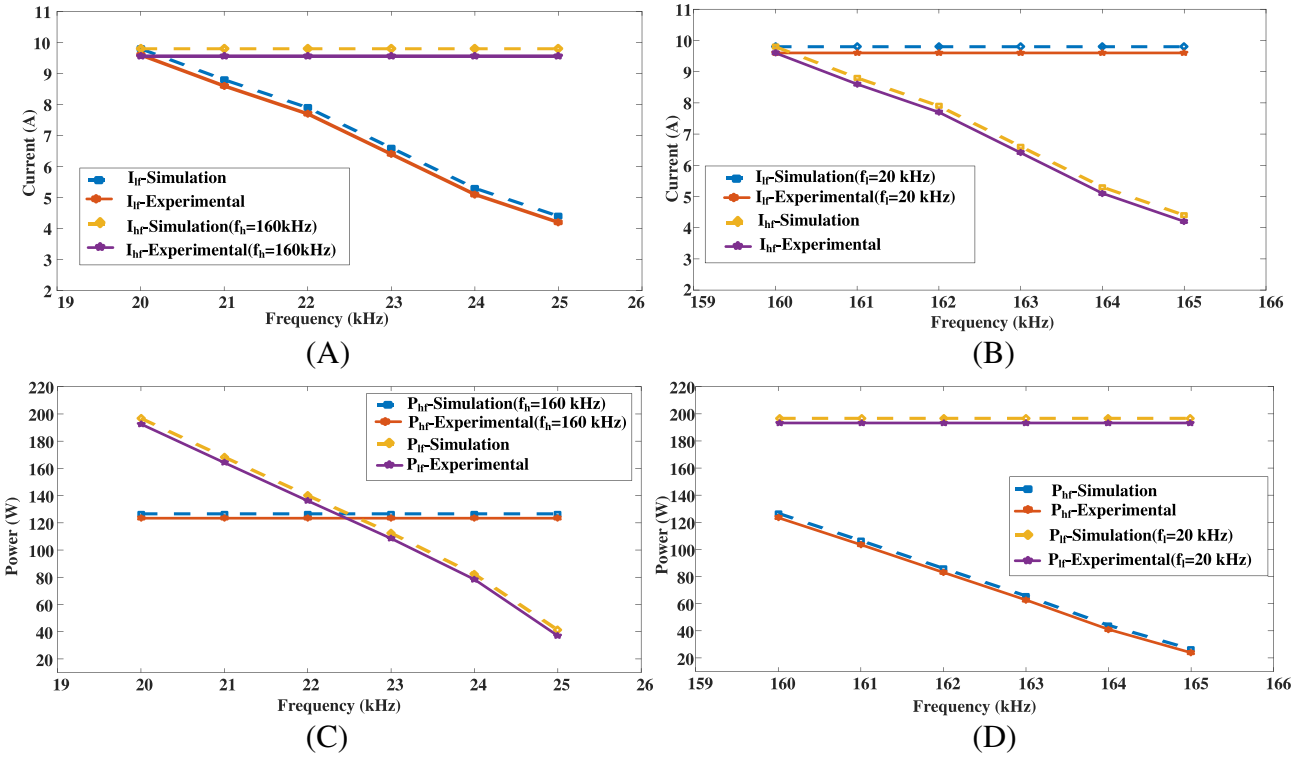

FIGURE 17 Low- and high-frequency output current and power control. (A) Load current variation with f_l. (B) Load current variation with f_h. (C) Load power variation with f_l. (D) Load power variation with f_h

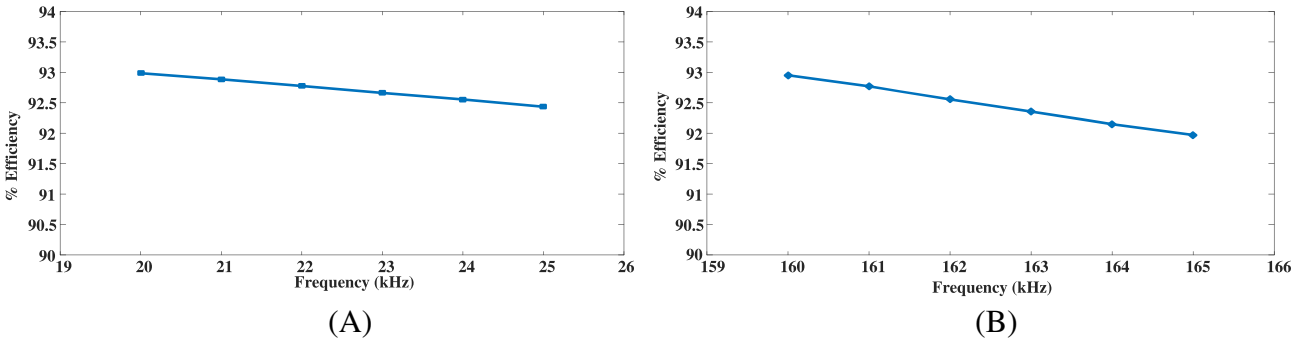

FIGURE 18 Efficiency curves. (A) Efficiency versus low frequency (f_l). (B) Efficiency versus high frequency (f_h)

$$\eta = \frac{P_o}{P_{in}} \tag{23}$$

The overall efficiency versus low and high switching frequencies are shown in Figure 18A,B, respectively. The overall efficiency of the proposed converter topology remains significantly high for both switching frequency variations. Thermal images of steel and aluminum vessels at different load currents are shown in Figures 19 and 20. Thermal imager (CHAUVIN ARNOUX-C.A1950) has been used. Thermal images of steel vessel at low-frequency currents of 4, 5, and 6.92 A are shown in Figure 19A–C, respectively. However these low-frequency currents cannot generate heat in aluminum vessel due to its lower values of permeability and equivalent resistance. Hence, the proposed inverter configuration powers the aluminum vessel load with high-frequency currents. Thermal images of aluminum vessel at high-frequency currents of 4, 5, and 6.96 A are shown in Figure 20A–C, respectively. From these figures, it is observed that aluminum vessel also gets heated, and hence, the proposed converter configuration is suitable for both steel and aluminum vessels.

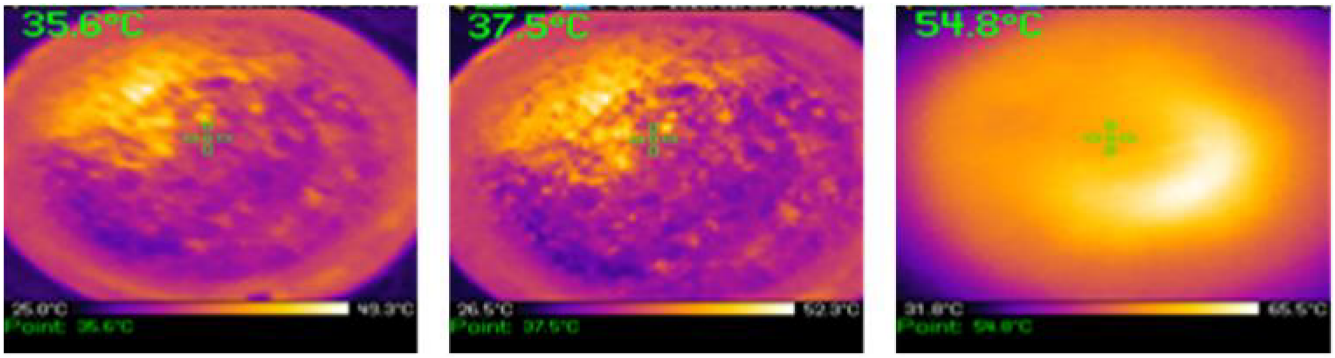

FIGURE 19 Steel vessel thermal images at $f_l = 20$ kHz. (A) $i_{lfrms} = 4$ A. (B) $i_{lfrms} = 5$ A. (C) $i_{lfrms} = 6.92$ A

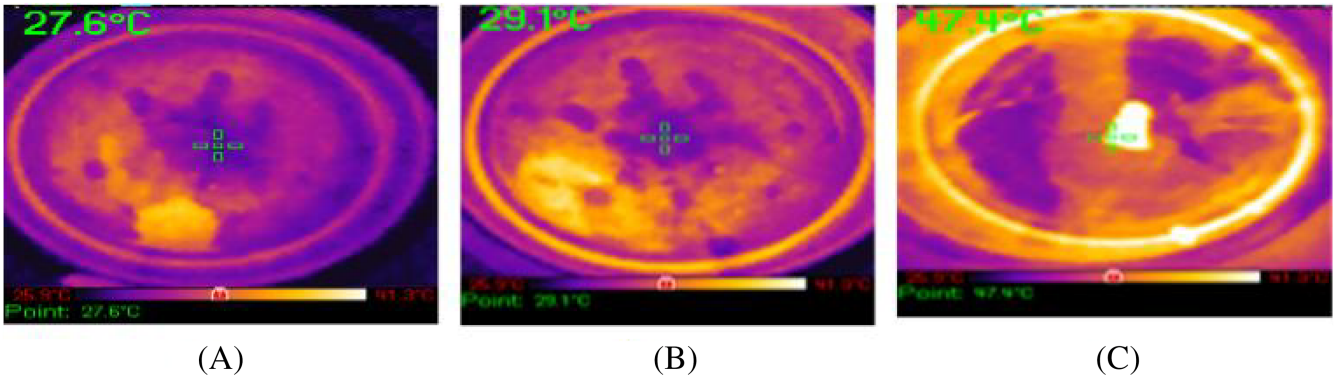

FIGURE 20 Aluminum vessel thermal images at $f_h = 160$ kHz. (A) $i_{hfrms} = 4$ A. (B) $i_{hfrms} = 5$ A. (C) $i_{hfrms} = 6.96$ A

In the proposed converter configuration, as integrated leg is used for both rectification and inversion, the number of diodes is reduced. The power factor is almost unity and the output voltage is boosted. It has higher conversion efficiency and the converter configuration can be extended for more number of loads, with one additional inverter leg per load. In Sarnago et al.[34] also the component count is similar. However, in Sarnago et al.[34] mechanical relays are used which increases the system cost and reducing the performance. Hence, with reduced component count, high efficiency and two different IH load powering capability the proposed converter is cost-effective.

6 | CONCLUSIONS

The proposed single-stage AC–AC resonant converter for different material induction cooking applications has been implemented. Inverter legs are operated at two different frequencies suitable for two different material cooking vessels. The low-frequency leg is common for both rectification and inversion operation. Low frequency of 20 kHz is used for steel vessel and high frequency of 160 kHz is used for aluminum vessel. Independent output power control is achieved by pulse frequency control. The number of switching devices is two per load. In this configuration, overall efficiency of >93% is achieved at full load. Output power control is achieved using pulse frequency control modulation technique. The salient features of the proposed converter are suitability for different material IH loads, single-stage AC–AC conversion, boost operation, high power factor, independent power control, soft switching operation and high efficiency. This converter offers advantages like single-stage AC–AC conversion, high power factor, DC-link voltage boost operation, low component count, suitability for different material vessels, independent power control and high efficiency.

ACKNOWLEDGMENT

The authors would like to thank Department of Science and Technology, Government of India, for the financial support under the SERB-CRG scheme (CRG/2018/4568, 09.05.2019) granted to Dr. S. Porpandiselvi.

DATA AVAILABILITY STATEMENT

The data that support the findings of this study are available from the corresponding author upon reasonable request.

ORCID

Srinivas Khatroth https://orcid.org/0000-0003-3227-0139
Porpandiselvi Shunmugam https://orcid.org/0000-0002-0168-2141

REFERENCES

1. Lucía O, Maussion P, Dede EJ, Burdío JM. Induction heating technology and its applications: past developments, current technology, and future challenges. *IEEE Trans Ind Electron*. 2013;61(5):2509-2520.
2. Meng L, Cheng KWE, Chan K. W. Systematic approach to high-power and energy-efficient industrial induction cooker system: Circuit design, control strategy, and prototype evaluation. *IEEE Trans Power Electron*. 2011;26(12):3754-3765.
3. Vishnuram P, Ramachandiran G, Ramasamy S, Dayalan S. A comprehensive overview of power converter topologies for induction heating applications. *Int Trans Electr Energy Syst*. 2020;30:e12554.
4. Kumar A, Sadhu M, Das N, Sadhu PK, Roy D, Ganguly A. A survey on high-frequency inverter and their power control techniques for induction heating applications. *J Power Technol*. 2017;97(3):201-213.
5. Kim MB, Moon GW, Youn MJ. Simple implementation of control gate signals for the interleaved LLC resonant converter for high current application. *Int J Circ Theory Appl*. 2011;39(12):1275-1283.
6. Ahmed T, Ogura K, Chandhaket S, Nakaoka M. Asymmetrical duty cycle controlled edge resonant soft switching high frequency inverter for consumer electromagnetic induction fluid heater. *Autom ATKAAF*. 2003;44(1-2):21-26.
7. Burdio JM, Barragan LA, Monterde F, Navarro D, Acero J. Asymmetrical voltage-cancellation control for full-bridge series resonant inverters. *IEEE Trans Power Electron*. 2004;19(2):461-469.
8. Chiu HJ, Lo YK, Lee TP, Chuang CC, Mou SC. A single-stage phase-shifted full-bridge AC/DC converter with variable frequency control. *Int J Circ Theory Appl*. 2010;38(8):867-879.
9. Lucia O, Burdio JM, Millan I, Acero J, Barragan L. A. Efficiency-oriented design of ZVS half-bridge series resonant inverter with variable frequency duty cycle control. *IEEE Trans Power Electron*. 2010;25(7):1671-1674.
10. Kim MB, Park KB, Youn M. J. A novel single-stage AC–DC converter with quasi-resonant zero-voltage-switching for high power factor and high efficient applications. *Int J Circ Theory Appl*. 2011;39(7):733-749.
11. Shen J, Ma H, Yan W, Hui J, Wu L. *PDM and PSM hybrid power control of a series-resonant inverter for induction heating applications*. Singapore: IEEE; 2006:1-6.
12. Sarnago H, Lucia O, Mediano A, Burdio J. M. Class-D/DE dual-mode-operation resonant converter for improved-efficiency domestic induction heating system. *IEEE Trans Power Electron*. 2012;28(3):1274-1285.
13. Lucia O, Burdio JM, Millan I, Acero J, Puyal D. Load-adaptive control algorithm of half-bridge series resonant inverter for domestic induction heating. *IEEE Trans Indust Electron*. 2009;56(8):3106-3116.
14. Burdio JM, Monterde F, Garcia JR, Barragan LA, Martinez A. A two-output series-resonant inverter for induction-heating cooking appliances. *IEEE Trans Power Electron*. 2005;20(4):815-822.
15. Forest F, Labouré E, Costa F, Gaspard J. Y. Principle of a multi-load/single converter system for low power induction heating. *IEEE Trans Power Electron*. 2000;15(2):223-230.
16. Papani SK, Neti V, Murthy B. K. Dual frequency inverter configuration for multiple-load induction cooking application. *IET Power Electron*. 2015;8(4):591-601.
17. Kumar S, Vishwanathan N, Bhagwan KM. Buck-boost interleaved inverter configuration for multiple-load induction cooking application. *J Electr Eng Technol*. 2015;10(1):271-279.
18. Lucia O, Carretero C, Burdio JM, Acero J, Almazan F. Multiple-output resonant matrix converter for multiple induction heaters. *IEEE Trans Ind Appl*. 2012;48(4):1387-1396.
19. Millan I, Puyal D, Burdio J, Acero J, Llorente S. *Resonant inverter topology for all-metal domestic induction heating*. Vigo, Spain: IEEE; 2007:913-918.
20. Hirokawa T, Hiraki E, Tanaka T, Okamoto M, Nakaoka M. *The practical evaluations of time-sharing high-frequency resonant soft-switching inverter for all metal IH cooking appliances*. Montreal, QC, Canada: IEEE; 2012:3302-3307.
21. Hirokawa T, Okamoto M, Hiraki E, Tanaka T, Nakaoka M. *A novel type time-sharing high-frequency resonant soft-switching inverter for all metal IH cooking appliances*. Melbourne, VIC, Australia: IEEE; 2011:2526-2532.
22. Yonemori H, Kobayashi M. *On the heating characteristic and magnetic flux of a double-coil drive type induction heating cooker*. Paris, France: IEEE; 2006:2488-2493.
23. Han W, Chau K, Jiang C, Liu W. All-metal domestic induction heating using single-frequency double-layer coils. *IEEE Trans Magn*. 2018;54(11):1-5.

24. Millan I, Burdío J, Acero J, Lucía O, Llorente S. Series resonant inverter with selective harmonic operation applied to all-metal domestic induction heating. *IET Power Electron*. 2011;4(5):587-592.
25. Park HP, Jung JH. Load-adaptive modulation of a series-resonant inverter for all-metal induction heating applications. *IEEE Trans Ind Electron*. 2018;65(9):6983-6993.
26. Sarnago H, Lucia O, Mediano A, Burdio JM. Direct AC–AC resonant boost converter for efficient domestic induction heating applications. *IEEE Trans Power Electron*. 2013;29(3):1128-1139.
27. Mishima T, Nakagawa Y, Nakaoka M. A bridgeless BHB ZVS-PWM AC–AC converter for high-frequency induction heating applications. *IEEE Trans Ind Appl*. 2015;51(4):3304-3315.
28. Gomes RCM, Vitorino MA, Acevedo-Bueno DA, Corrêa MBdR. Multiphase resonant inverter with coupled coils for AC–AC induction heating application. *IEEE Trans Ind Appl*. 2019;56(1):551-560.
29. Lee SW, Do HL. Efficient bridgeless PFC converter with reduced voltage stress. *Int J Circ Theory Appl*. 2016;44(7):1455-1467.
30. Mishima T, Morinaga S, Nakaoka M. Single-stage ZVS-PWM AC–AC power converter using all SiC power module for high-frequency induction heating applications. *Electrical Engineering in Japan*. 2017;201(3):69-76.
31. Mishima T, Sakamoto S, Ide C. ZVS phase-shift PWM-controlled single-stage boost full-bridge AC–AC converter for high-frequency induction heating applications. *IEEE Trans Ind Electron*. 2016;64(3):2054-2061.
32. Sarnago H, Lucia O, Mediano A, Burdio JM. Design and implementation of a high-efficiency multiple-output resonant converter for induction heating applications featuring wide bandgap devices. *IEEE Trans Power Electron*. 2013;29(5):2539-2549.
33. Pérez-Tarragona M, Sarnago H, Lucía Ó, Burdío JM. Design and experimental analysis of PFC rectifiers for domestic induction heating applications. *IEEE Trans Power Electron*. 2017;33(8):6582-6594.
34. Sarnago H, Lucia O, Burdio JM. *Multiple-output boost resonant inverter for high efficiency and cost-effective induction heating applications*. Long Beach, CA, USA: IEEE; 2016:1040-1044.
35. Sarnago H, Guillén P, Burdío JM, Lucia O. Multiple-output ZVS resonant inverter architecture for flexible induction heating appliances. *IEEE Access*. 2019;7:157,046-157,056.

How to cite this article: Khatroth S, Shunmugam P. Single-stage pulse frequency controlled AC–AC resonant converter for different material vessel induction cooking applications. *Int J Circ Theor Appl*. 2021;49(9): 2865-2884. doi:10.1002/cta.3042